Spin state of iron in $I\bar{4}2d$-type Mg$_2$SiO$_4$ at ultrahigh pressures

Tianqi Wan [1], Yang Sun [1,2,3] and Renata M. Wentzcovitch [1,4,5,6,*]

[1]*Department of Applied Physics and Applied Mathematics, Columbia University, New York, New York 10027, USA*
[2]*Department of Physics, Xiamen University, Xiamen 361005, China*
[3]*Department of Physics, Iowa State University, Ames, IA 50011, USA*
[4]*Department of Earth and Environmental Sciences, Columbia University, New York, New York 10027, USA*
[5]*Lamont-Doherty Earth Observatory, Columbia University, Palisades, New York 10964, USA*
[6]*Data Science Institute, Columbia University, New York, New York 10027, USA*

At extreme pressures of approximately 500 GPa—conditions characteristic of the deep interiors of super-Earths—the combination of NaCl-type MgO and postperovskite-type MgSiO$_3$ (PPv) has been reported to produce a postpost-perovskite (PPPv) phase of Mg$_2$SiO$_4$ with an $I\bar{4}2d$ symmetry. This PPPv silicate is proposed as the primary mantle silicate in these massive rocky exoplanets. Understanding the fundamental properties of PPPv, particularly in solid solutions with Fe$_2$SiO$_4$, is crucial for insight into the interior dynamics and compositions of such planets. In this study, we conduct an *ab initio* investigation of the properties of Fe^{2+}-bearing PPPv at pressures ranging 400 GPa–1 TPa. Given the localized nature of 3d electrons in iron, we employ the LDA + U_{SC} method alongside conventional density functional theory functionals to probe the electronic structure of this system. The dependence of the Hubbard parameter U on volume and spin state is carefully evaluated. Furthermore, we systematically explore the effects of pressure, temperature, and structural variations on the spin state of iron in Fe^{2+}-bearing PPPv, providing valuable data to improve mantle modeling for super-Earth-type exoplanets.

I. INTRODUCTION

More than 5500 exoplanets have been reported since the extraordinary discovery of a Jupiter mass planet around a Sun-like star, Pegasi 51 [1]. Among these exoplanets, super-Earth-type planets are arguably the most interesting. Investigating the distinctions between these exoplanets and our own Earth has become a vital pursuit, as it can deepen our understanding of the formation processes of planetary systems and offers insight into the search for habitable worlds. In this endeavor, researchers have initially approached the study by assuming compositions akin to Earth and other terrestrial planets within our solar system, gradually introducing complexity as our knowledge advances [2].

MgSiO$_3$ perovskite (Pv) is the major constituent of the Earth's mantle, and its highest-pressure polymorph in the mantle is postperovskite (PPv) [3–5]. In super-Earths, other forms of aggregation of MgO and SiO$_2$ stabilized by higher pressures and temperatures in their mantles are expected. Several postpostperovskite (PPPv) minerals like $I\bar{4}2d$-tpye Mg$_2$SiO$_4$ and $P2_1/c$-type MgSi$_2$O$_5$ have been reported recently by *ab initio* calculations [6–10]. So far, these PPPv phase transitions have not been confirmed experimentally due to the extremely high pressures. Also, the presence of iron affects several properties significantly, such as elastic and seismic properties [11–14] and electrical and thermal conductivity [15–17]. Here, we focus on the characterization of the Fe^{2+}-bearing $I\bar{4}2d$-type Mg$_2$SiO$_4$ at ultrahigh pressure and offer predictions for high-pressure experiments.

As reported in previous research [12], iron's spin state directly affects the mineral's elastic, transport, and rheological properties. The presence of localized 3d electrons in iron requires methods beyond standard density functional theory (DFT) to address their strongly correlated nature [18–22]. Among these, the widely adopted DFT + U method introduces the Hubbard correction to standard DFT calculations, enhancing the accuracy of results [23,24]. However, the reliability of DFT + U outcomes critically hinges on the appropriate determination of the Hubbard parameter U, which should be derived self-consistently and be volume- and spin-state dependent [12,19,25–30].

We study iron spin states, including high spin (HS), intermediate spin (IS), and low spin (LS) states, in $I\bar{4}2d$-type Mg$_2$SiO$_4$ and corresponding electronic structure using LDA + U_{SC} and conventional DFT methods. The dependence of U on pressure, volume, and spin state is carefully considered in the system at ultrahigh pressures. A local distortion in the LS state, which is important for its stabilization, has also been included. Also, we use the quasiharmonic approximation (QHA) [31] to compute the vibrational free energy.

This paper is organized as follows. In Sec. II, we provide a comprehensive account of the methods employed in this study. Section III presents our results for the electronic structure of different spin states, their respective free energies, and the spin phase diagram. Section IV presents our conclusions.

---

*Contact author: rmw2150@columbia.edu

II. METHOD

A. *Ab initio* calculations

Ab initio calculations are done with the QUANTUM ESPRESSO code [32,33]. The local density approximation (LDA) and LDA + U_{SC} calculations use Vanderbilt's ultrasoft pseudopotentials [34] with valence electronic configurations $3s^2\,3p^6\,3d^{6.5}\,4s^1\,4p^0$, $3s^2\,3p^1$, and $2s^2\,2p^4$ for Fe, Si, and O, respectively. The pseudopotential for Mg was generated by the von Barth–Car method using five configurations $3s^2\,3p^0$, $3s^1\,3p^1$, $3s^1\,3p^{0.5}\,3d^{0.5}$, $3s^1\,3p^{0.5}$, and $3s^1\,3d^1$ with decreasing weights 1.5, 0.6 0.3 0.3, and 0.2, respectively. These pseudopotentials for Fe, Mg, Si, and O were generated, tested, and previously used in numerous works, e.g., in Umemoto *et al.* [5–7,10,35]. Plane-wave energy cutoffs are 100 and 800 Ry for electronic wave functions and spin-charge density and potentials, respectively. In structural optimization, the irreducible Brillouin zone of the 28-atom cells is sampled by a $4 \times 4 \times 4$ Monkhorst-Pack mesh [36]. Finer **k**-point grids ($6 \times 6 \times 6$) are used to calculate the projected density of states and charge density. Effects of larger energy cutoff and denser **k**-point sampling on calculated properties are insignificant. The convergence thresholds are 0.01 eV/Å for all components (f_x, f_y, and f_z) of all forces, including atomic forces and averaged forces in the supercell, and 1×10^{-7} eV for the total energy of the supercell, 28 atoms in this work.

In our LDA + U_{SC} calculations, we apply the Hubbard correction [23] specifically to the Fe-$3d$ states. To compute the Hubbard parameter U, we utilize density-functional perturbation theory (DFPT) [37]. The convergence threshold for the response function is 1×10^{-6} eV. We employed an automated iterative scheme to ensure the self-consistency of the U_{SC} parameter and optimize the structure and spin state simultaneously [29]. Initially, we consider an empirical U value of 4.3 eV and compute the energies associated with all possible occupation matrices for the HS ($S = 2$), IS ($S = 1$), and LS ($S = 0$) states, resulting in a total of 65 possibilities. Among these, we select the electronic configuration, i.e., the occupation matrix with the lowest energy, for further structural optimization of lattice parameters and atomic positions. During the structural optimization, a new U parameter is recalculated. This process continues until mutual convergence of the structure and U parameter is achieved within 0.01 eV for the U parameter (see, e.g., [29]) and the above-mentioned convergence criteria for structural optimizations [30,38]. The volume dependence of U_{SC} is crucial in this study due to the broad pressure range considered and its key role in determining Gibbs free energy and their differences among spin states.

Phonon calculations are performed in 224-atom supercells using the finite-displacement method with the PHONOPY code [39] and LDA + U_{SC} forces obtained with the QUANTUM ESPRESSO. To obtain the vibrational density of states (VDOS), we employ a q-point mesh of $12 \times 12 \times 12$. The vibrational contribution to the free energy is then calculated using the quasiharmonic approximation (QHA) [31] with the QHA code [40].

B. Free energy calculations

Since we expect high temperatures >4000 K in the mantle of super-Earths, it is necessary to include the vibrational and electronic entropy to compute free energies. Recently, it has been highlighted [41,42] that including the electronic entropy within the Mermin functional [43,44] in a continuum of temperatures T_{el} is important for calculating the thermodynamic properties. In this study, we perform the static calculation within a continuum of electronic temperatures T_{el}. We sample electronic temperatures from 1000 to 7000 K with a spacing of 2000 K, employing temperature interpolations. Combining the vibrational entropy S_{vib}, obtained from phonon dispersion calculations, with the electronic entropy, we compute the Gibbs free energy for all three spin states utilizing the QHA. Obviously, $T_{el} = T$ when the system is in thermodynamic equilibrium. A common expression for the free energy in this case is

$$F(V, T, T_{el}) = F_{static}(V, T_{el}) + F_{vib}(V, T, T_{el}), \quad (2a)$$

where

$$F_{static}(V, T_{el}) = F_{Mermin}(V, T_{el}) \quad (2b)$$

is the total Mermin free energy at volume V. Here,

$$F_{Mermin}(V, T_{el}) = E_{static}(V, T_{el}) - T_{el}S_{el}(V, T_{el}), \quad (2c)$$

where $E_{static}(V, T_{el})$ is the self-consistent energy with orbital occupancies:

$$f_{ki}(V, T_{el}) = \frac{1}{\exp\left(\frac{\hbar(E_{ki}-E_F)}{k_B T_{el}}\right) + 1}, \quad (2d)$$

with E_{ki} being the one-electron energy of an orbital with wave number **k** and band index i, and E_F being the Fermi energy. The electronic entropy is

$$S_{el} = -k_B \sum_{k,i} [(1 - f_{ki})\ln(1 - f_{ki}) + f_{ki}\ln(f_{ki})]. \quad (2e)$$

The vibrational energy is

$$F_{vib}(V, T, T_{el}) = \frac{1}{2} \sum_{q,s} \hbar\omega_{q,s}(V, T_{el} = 0)$$
$$+ k_B T \sum_{q,s} \ln\left\{1 - \exp\left[-\frac{\hbar\omega_{q,s}(V, T_{el})}{k_B T}\right]\right\}, \quad (2f)$$

where $\omega_{q,s}(V)$ is the vibrational frequency of noninteracting phonons with wave number **q** and polarization index s.

III. RESULTS

A. HS and IS Fe^{2+} in Fe^{2+}-bearing PPPv

The crystal structure of $I\bar{4}2d$ Mg_2SiO_4 is essential to understanding the electronic structure of the Fe^{2+} ion. It exhibits a body-centered-tetragonal phase, which shares the same cation configuration as Zn_2SiO_4-II [45]. However, significant differences exist in the arrangement of oxygen atoms. Mg_2SiO_4 adopts a more densely packed structure compared to Zn_2SiO_4-II. The Zn and Si atoms in Zn_2SiO_4-II are tetrahedrally coordinated. In contrast, Mg and Si atoms in Mg_2SiO_4 are coordinated by oxygens eightfold. MgO_8 and SiO_8 polyhedra exhibit striking similarities, with triangular faces forming pentagonal caps. The packing of Mg- and
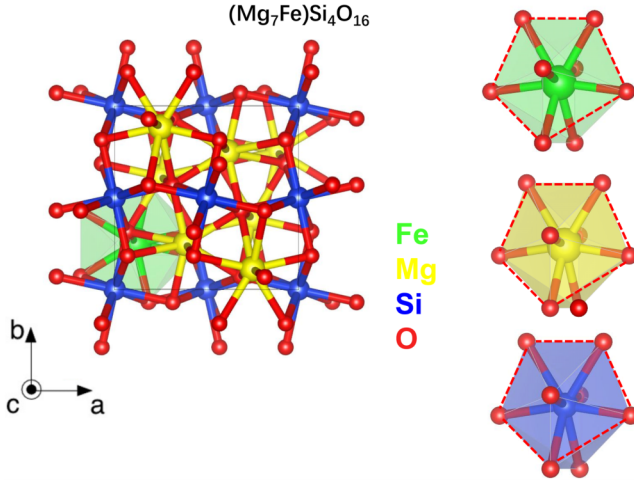
FIG. 1. Crystal structure of Fe^{2+}-bearing $I\bar{4}2d$-type Mg$_2$SiO$_4$ at 1 TPa. Green, yellow, blue, and red spheres denote Fe, Mg, Si, and O ions.

Si-centered polyhedra occurs through various edge- and face-sharing arrangements. Specifically, Si polyhedra share their edges, while Mg polyhedra share their faces. The crystal structures of $I\bar{4}2d$-type Mg$_2$SiO$_4$ together with the corresponding MO_8 (M = Mg, Fe, Si) polyhedra are shown in Fig. 1. It is important to point out that the difference of average bond lengths between MgO$_8$ and SiO$_8$ is also small, shown in Table I, $\overline{\text{Mg}-\text{O}} = 1.60$ Å and $\overline{\text{Si}-\text{O}} = 1.57$ Å.

In the context of Fe^{2+} substitution within $I\bar{4}2d$-type Mg$_2$SiO$_4$, our focus is primarily on the state of ferrous iron. However, it is important to acknowledge that ferric iron (Fe^{3+}) can concurrently enter through coupled substitutions at the Mg and Si sites, as Mg and Si in this structure should be disordered [46–48]. However, locally, we expect the Fe^{2+} coordination to be well described by the one adopted here. Fe^{2+} in the Mg site can be in HS ($d_\uparrow^5 d_\downarrow^1$), IS ($d_\uparrow^4 d_\downarrow^2$), or LS ($d_\uparrow^3 d_\downarrow^3$) states. Using the LDA + U_{SC} method, all of these spin states have been carefully investigated. Figure 5(a) showcases the self-consistent Hubbard parameters. Notably, the HS state consistently exhibits lower U values than the LS states, a trend observed in ferropericlase [42,49]. This trend is also found in FeO where the LS state of Fe^{2+} always shows the largest self-consistent U value, regardless of crystal structure [29]. The U_{SC} values exhibit variations of approximately 1 eV within the volume range inspected, corresponding to 400 GPa < P < 1000 GPa. Thus, in addition to the dependence on electronic configuration, the Hubbard parameter manifests a

significant volume dependence. This phenomenon was initially observed in the study of the spin crossover of Fe^{2+} in ferropericlase [30].

The projected density of states (PDOS) and charge density of HS and IS at 1 TPa are shown in Figs. 2(a) and 2(b). In the HS state, all spin-up orbitals are fully occupied by five electrons, while the remaining electron occupies the spin-down d_{xy} orbital, producing the $d_\uparrow^5 d_\downarrow^1$ electronic configuration with $S = 2$. It is important to note that the FeO$_8$ coordination in this case does not form a perfect cube. The specific coordination and the associated Jahn–Teller distortion lead to the complete removal of the typical d-level degeneracy, i.e., a triplet (the t_{2g} states) and a doublet (the e_g state) in octahedral or cubic environments, as seen in B1- and B2-ferropericlase [42]. Instead, the five $3d$ orbitals in this system become completely nondegenerate, forming five a_{1g} singlets. As shown in Fig. 2(c), the d_{xy} orbital points away from the neighboring negatively charged oxygen atoms, while the $d_{x^2-y^2}$ points toward them, thereby exhibiting the highest energy. The eightfolded coordination similar to that in B2 ferropericlase [42] also leads to the stability of intermediate spin (IS) state. In the IS state, four electrons occupy the d_{xy}, d_{xz}, d_{yz}, and d_{z^2} orbitals in the spin-up channel, while the remaining two electrons occupy the spin-down d_{xy} and d_{yz} orbitals. This leads to an electronic configuration of $d_\uparrow^4 d_\downarrow^2$ with a total spin $S = 1$. Additionally, as the spin state changes to the IS state, the energy of the d_{yz} and d_{xz} orbitals in the spin-up channel develop into a doublet, as shown in Figs. 2(b) and 2(h).

B. LS Fe^{2+} in the Fe^{2+}-bearing PPPv

Furthermore, we have also considered the LS state. In the LS state, the electron occupying the d_{z^2} orbital with spin up in the IS state can fill the d_{xz} orbital with spin down, resulting in the LS state with an electronic configuration of $d_\uparrow^3 d_\downarrow^3$. Despite full structural optimization, this LS state still exhibits imaginary phonon instabilities, as shown in Fig. 3(c), indicating that it is settled in an unstable equilibrium atomic configuration. To address this issue, we introduced a displacement mode corresponding to the largest imaginary frequency around the gamma point and performed structural optimization after such displacement. Another displacement mode corresponding to the second largest imaginary frequency around the gamma point yields the same distorted structure. Figure 3(d) demonstrates that this newly distorted LS state is dynamically stable, as the phonon instabilities are no longer present.

The investigation of these two competing LS states deserves closer attention. The atomic structures of these two states show a great resemblance, including the eightfold coordination. The main difference between them lies in the iron position. Figures 3(a) and 3(b) show the atomic arrangements around iron in these two states. By displacing iron along [001] and [110] from the undistorted LS state, several Fe-O bond lengths change. In the undistorted LS state, there are four pairs of Fe-O band lengths that split upon such displacements. Specifically, four out of the eight bonds shorten, and four lengthen. Notably, one of the two longest Fe-O bonds in the undistorted LS state shortens from 1.72 to 1.6 Å at 1 TPa. Table I shows an average decrease of approximately 0.2% in the Fe-O bond length between the undistorted LS state and

TABLE I. Average bond length among different spin states at 1 TPa.

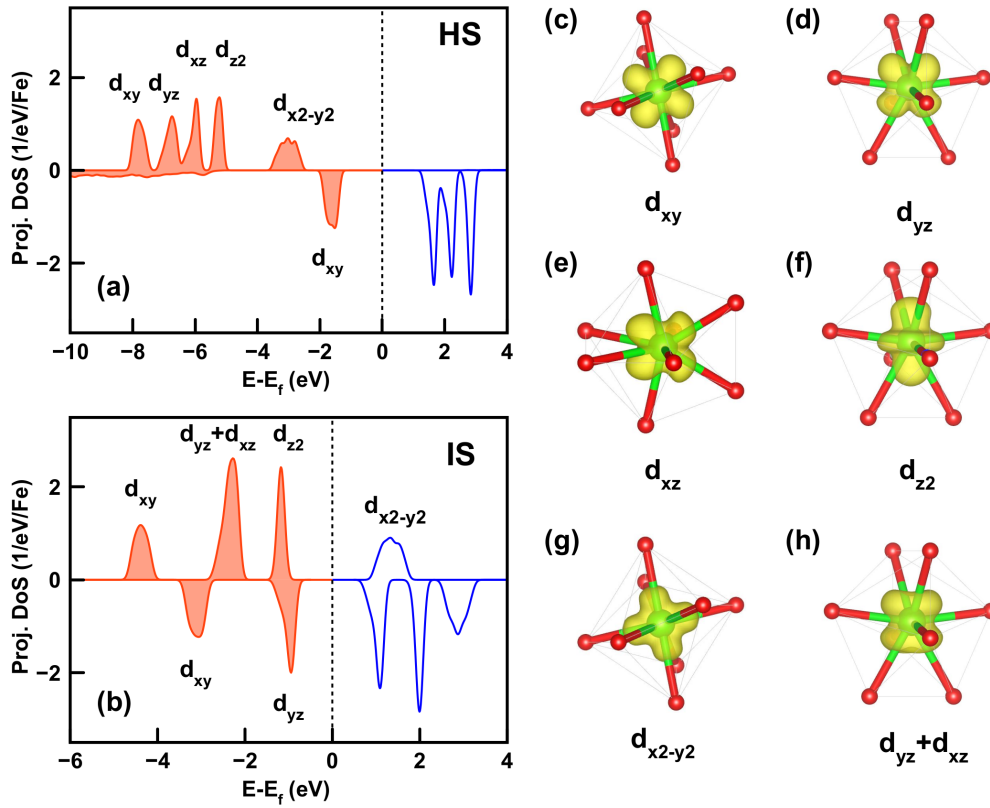| Average bond length (Å)	HS	IS	Undistorted LS	Distorted LS
Fe-O	1.640	1.641	1.637	1.640
Mg-O	1.60	1.60	1.60	1.60
Si-O	1.57	1.57	1.57	1.57

FIG. 2. Projected density of states (PDOS) at 1 TPa for Fe $3d$ orbitals in (a) HS and (b) IS. Panels (c)–(g) present the charge density (yellow) for the different occupied orbitals in HS. Panel (h) presents the charge density (yellow) for the occupied doublet orbital in IS.
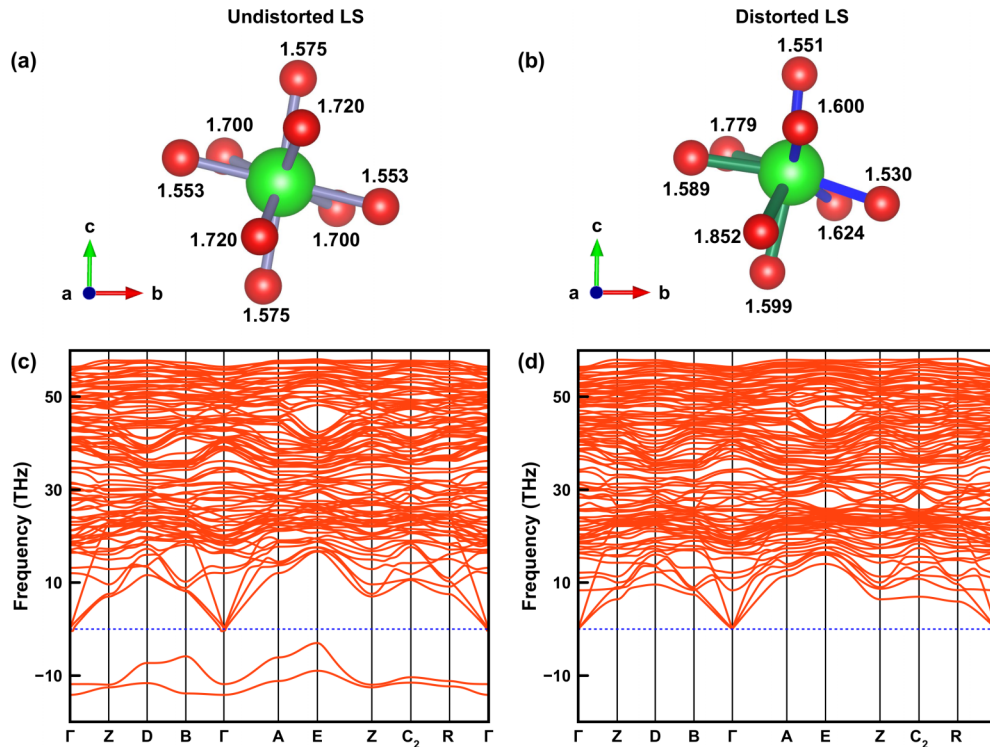

FIG. 3. Local atomic configurations around iron and phonon dispersion at 1 TPa in (a) and (c) undistorted LS state and (b) and (d) distorted LS state. Numbers next to oxygens are Fe-O bond lengths (in Å). The [100] direction is pointing out of the paper.
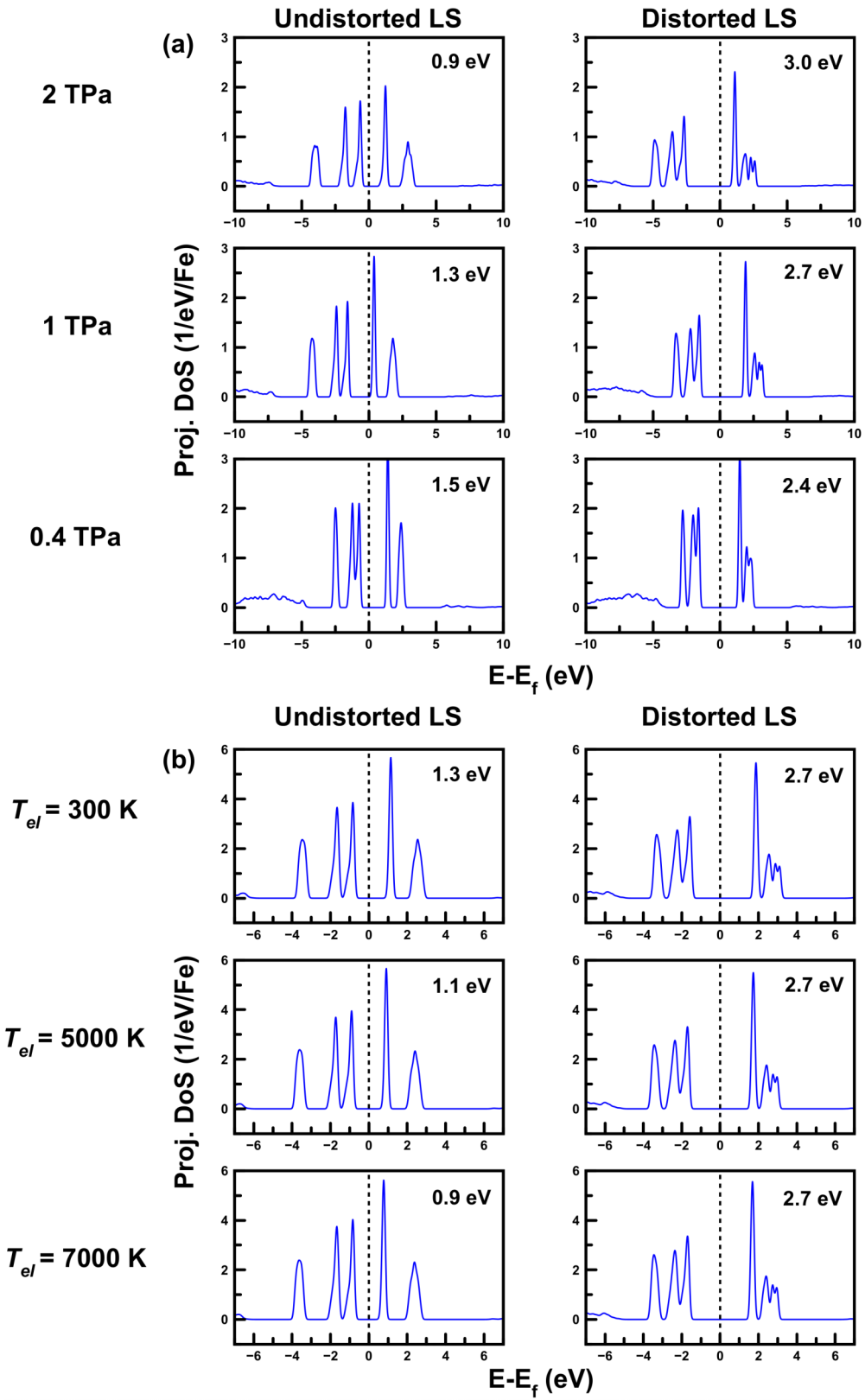
FIG. 4. Projected density of states (PDOS) of two competing LS state at (a) different pressures; (b) different T_{el}. The numbers in each panel represent the band gap (in eV).
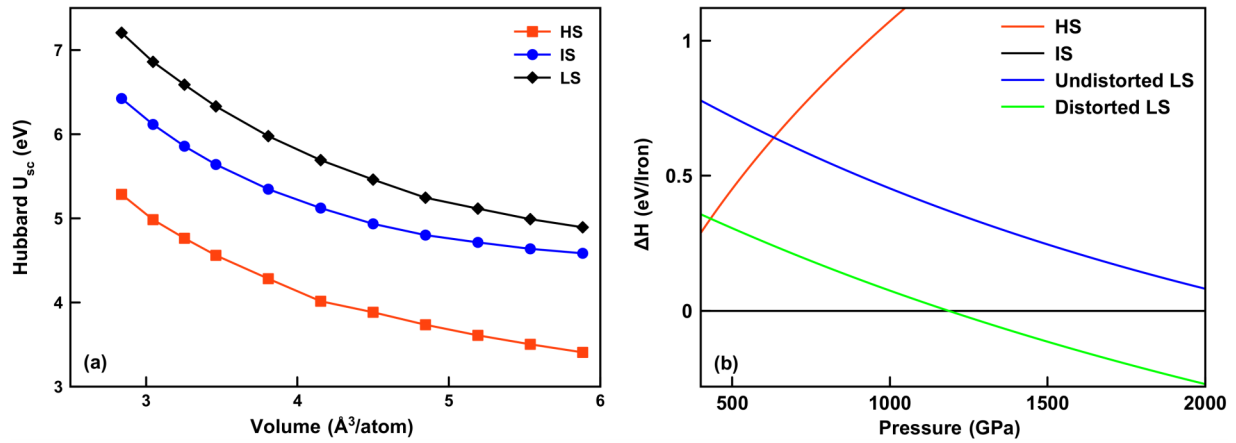
FIG. 5. (a) The self-consistent Hubbard parameters U vs volume. (b) Relative enthalpy (ΔH_i) of Fe^{2+}-bearing $I\bar{4}2d$-type Mg_2SiO_4 in different spin states with respect to the IS state.

the HS or IS state. Such decrease in the Fe-O bond length is no longer present after the distortion occurs. Therefore, the average Fe-O bond length in the distorted LS state is nearly identical to that in the HS or IS state.

Despite the different Fe-O arrangements, the d-orbital occupancies of iron remain the same after the distortion. Figure 4 shows the projected density of states (PDOS) of the two competing LS states at different pressure and T_{el}. We note that the undistorted LS state is an insulator with an energy gap slightly larger than 1.5 eV at 0.4 TPa. As the pressure increases, the energy gap gradually decreases and approaches $\sim$0.9 eV at 2 TPa, indicating a tendency towards metallicity at higher pressures. However, the band gap increases to around 2.4 eV at 0.4 TPa in the distorted structure, and the influence of pressure will open the band gap. Furthermore, including the Mermin functional [43,44] provides a first glimpse of the electronic structure at higher temperatures which is more realistic for exoplanetary interiors. Similarly, the undistorted LS state remains an insulating state with an energy gap of $\sim$0.9 eV at T_{el} = 7000 K, and 1.3 eV at T_{el} = 300 K. The distortion enlarges the gap to $\sim$2.7 eV, which remains almost constant from T_{el} = 300 to 7000 K. Therefore, this distortion plays a crucial role in stabilizing not only the vibrational properties but also the insulating state against pressure and temperature.

C. Stability of IS Fe^{2+} in Fe^{2+}-bearing PPPv

Using the LDA + U_{SC} method, the enthalpies of Fe^{2+}-bearing PPPv with all spin states can be computed. The energy-volume results of each state are fitted using the third-order Birch-Murnaghan (BM) equation of state (EOS). The relative enthalpies (ΔH_i) of each spin state i (i = HS, IS, undistorted LS, and distorted LS) with respect to the IS state are plotted in Fig. 5(b). The distorted LS state consistently exhibits a lower enthalpy than the undistorted LS state throughout the investigated pressure range, indicating that the distorted LS state is energetically favorable. There is an enthalpy crossing observed at around 1190 GPa between the IS state and the distorted LS state.

We further analyze these states' stability at high temperatures by computing the vibrational density of states and the vibrational free energy using the QHA code [40]. Figure 6

displays the phonon density of states of different spin states ranging 400 GPa–2 TPa. The undistorted LS state exhibits imaginary frequencies at all pressures, indicating the necessity of the distortion to stabilize phonons in the LS state. This stabilization is also closely related to the stability of the insulating state. Furthermore, increasing pressure increases phonon frequencies in HS, IS, and distorted LS states. No imaginary frequencies are observed in the investigated pressure. Therefore, the HS, IS, and distorted LS states of Fe^{2+} in Fe^{2+}-bearing PPPv with x_{Fe} = 0.125 are dynamically stable at high temperatures. Figure 7(a) shows the relative Gibbs free energy (ΔG_i) of different spin states with respect to the IS state at various temperatures. Within this pressure range, the HS state consistently has a higher free energy, indicating that the HS state is not stable. As temperature increases, ΔG_{LS-IS} gradually increases, further stabilizing the IS state. On the other hand, pressure tends to stabilize the distorted LS state,
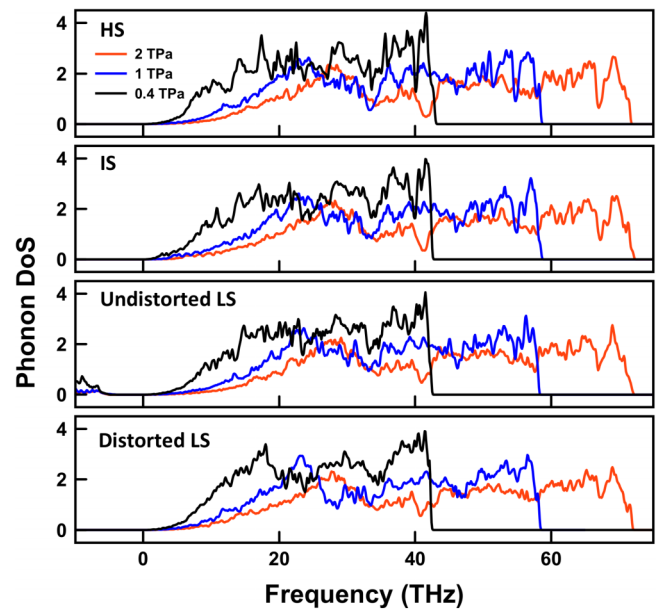

FIG. 6. Phonon density of state for Fe^{2+}-bearing $I\bar{4}2d$-type Mg_2SiO_4 with different spin states.
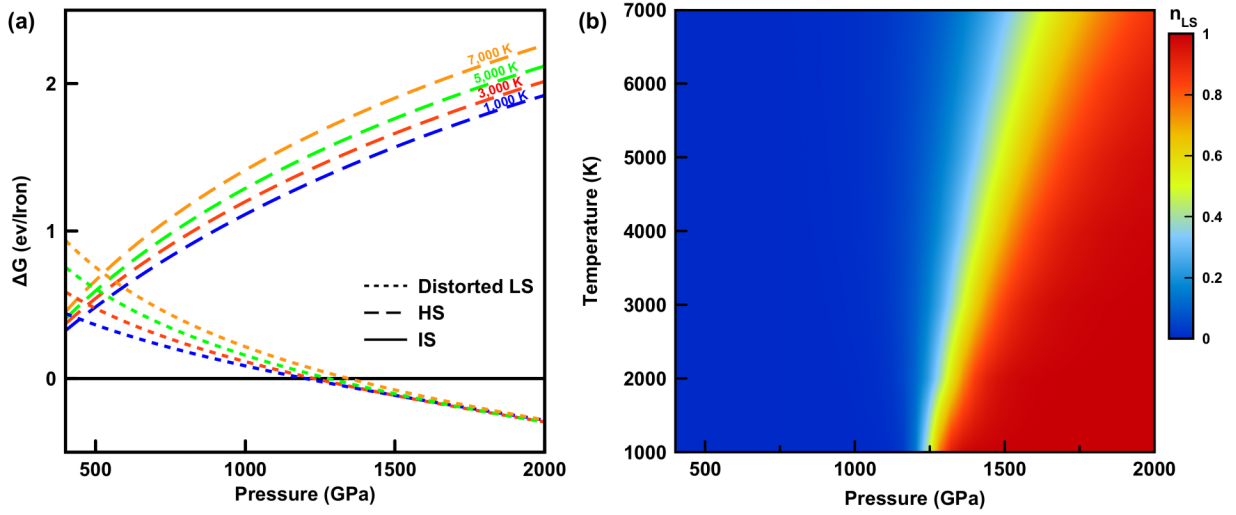
FIG. 7. (a) Relative Gibbs free energy (ΔG_i) of Fe^{2+}-bearing $I\bar{4}2d$-type Mg_2SiO_4 in each spin state with respect to the IS state. The black solid line corresponds to the IS state. Dashed and dotted lines correspond to the HS and distorted LS states, respectively. Colors denote different temperatures. (b) Stability fields of the distorted LS and IS states with magnetic entropy and configuration entropy contributions to the free energy taken into account.

which could induce a transition from the IS to the LS spin state. This would result in a positive Clapeyron if the IS-to-LS state change were a regular phase transition. However, as other pressure-induced spin states change within a single crystal structure, this is a crossover with a positive slope, as shown in Fig. 7(b).

To obtain the spin crossover diagram shown in Fig. 7(b), we added the non-negligible IS/LS configuration entropy and magnetic entropy contributions to the free energy [12,30]:

$$S_{\text{mag}} = k_B x_{\text{Fe}} (1-n) \ln [m(2S+1)],$$

where k_B is the Boltzmann constant, S is the total spin of iron ($S = 1$ for IS and $S = 0$ for LS), n is the fraction of LS iron, and m is the degeneracy of the electronic configuration [$m = 2$ for IS due to the doublet degeneracy shown in Fig. 2(b), and $m = 1$ for LS]. The magnetic entropy is nonzero for the IS state. Another important contribution is the configuration entropy associated with coexisting IS and LS irons:

$$S_{\text{conf}} = -k_B x_{\text{Fe}} [n \ln n + (1-n) \ln (1-n)].$$

With these considerations, the Gibbs free energy can be minimized with respect to the LS fraction n to give

$$n = \frac{1}{1 + m(2S+1)\exp\left\{\frac{\Delta G_{\text{LS-IS}}(P,T)}{k_B x_{\text{Fe}} T}\right\}},$$

where $\Delta G_{\text{LS-IS}}(P,T) = [G_{\text{LS}}(P,T) - G_{\text{IS}}(P,T)]$ is the Gibbs free energy difference between the LS and IS states, as shown in Fig. 7(a). The $n(P,T)$ diagram for PPPv with $x_{\text{Fe}} = 12.5\%$ is presented in Fig. 7(b). The IS-LS coexistence region broadens with increasing temperature. Notably, there is no sharp or discontinuous change in n, and thus it is a spin crossover.

IV. CONCLUSION

We have investigated the stability of various spin states of Fe^{2+} in Fe^{2+}-bearing $I\bar{4}2d$-type Mg_2SiO_4 at ultrahigh

pressures using LDA $+ U_{\text{SC}}$ calculations. In the HS state, with $S = 2$ and $d_\uparrow^5 d_\downarrow^1$ occupancy, we find all $3d$ orbitals to be singlets with a_{1g} symmetry. In the IS state with $S = 2$ and $d_\uparrow^4 d_\downarrow^2$ occupancy, a doublet consisting of d_{yz} and d_{xz} orbitals appears in the majority-spin channel. The LS state with $S = 0$ and $d_\uparrow^3 d_\downarrow^3$ occupancy exhibits imaginary phonon frequencies, indicating structural instability. Thus, a distortion is necessary for this LS state to stabilize vibrations and reduce the enthalpy. Phonon calculations confirm the dynamic stability of the HS, IS, and distorted LS states within the investigated pressure range. The IS state is the most stable state throughout the investigated pressure range, with no observed transitions between HS or LS states, irrespective of pressure and temperature.

Our calculations shed light on the significant influence of strong $3d$ electron localization and structural distortions on stabilizing the spin state in the Fe^{2+}-bearing PPPv system at ultrahigh pressures and temperatures. However, given the complexity of the problem, it will be important to consider further electron-phonon and phonon-phonon interactions in the future, as they likely play important roles in determining the behavior of the ferrous ion. Additionally, the possibility of iron atoms substituting the Si^{4+} site with a similar atomic environment in cation-disordered Mg_2SiO_4 and the inclusion of aluminum in this phase will greatly impact the electronic behavior of the system.

DATA AVAILABILITY

The data that support the findings of this article are openly available [51].

[1] M. Mayor and D. Queloz, A jupiter-mass companion to a solar-type star, Nature (London) **378**, 355 (1995).

[2] A. E. Doyle, E. D. Young, B. Klein, B. Zuckerman, and H. E. Schlichting, Oxygen fugacities of extrasolar rocks: Evidence for an earth-like geochemistry of exoplanets, Science **366**, 356 (2019).

[3] M. Murakami, K. Hirose, K. Kawamura, N. Sata, and Y. Ohishi, Post-perovskite phase transition in $MgSiO_3$, Science **304**, 855 (2004).

[4] A. R. Oganov and S. Ono, Theoretical and experimental evidence for a post-perovskite phase of $MgSiO_3$ in earth's D'' Layer, Nature (London) **430**, 445 (2004).

[5] T. Tsuchiya, J. Tsuchiya, K. Umemoto, and R. M. Wentzcovitch, Phase transition in $MgSiO_3$ perovskite in the earth's lower mantle, Earth Planet. Sci. Lett. **224**, 241 (2004).

[6] K. Umemoto, R. M. Wentzcovitch, and P. B. Allen, Dissociation of $MgSiO_3$ in the cores of gas giants and terrestrial exoplanets, Science **311**, 983 (2006).

[7] K. Umemoto and R. M. Wentzcovitch, Two-stage dissociation in $MgSiO_3$ post-perovskite, Earth Planet. Sci. Lett. **311**, 225 (2011).

[8] S. Q. Wu, M. Ji, C. Z. Wang, M. C. Nguyen, X. Zhao, K. Umemoto, R. M. Wentzcovitch, and K. M. Ho, An adaptive genetic algorithm for crystal structure prediction, J. Phys.: Condens. Matter **26**, 035402 (2013).

[9] H. Niu, A. R. Oganov, X. Q. Chen, and D. Li, Prediction of novel stable compounds in the Mg-Si-O system under exoplanet pressures, Sci. Rep. **5**, 18347 (2015).

[10] K. Umemoto, R. M. Wentzcovitch, S. Wu, M. Ji, C. Z. Wang, and K. M. Ho, Phase transitions in $MgSiO_3$ post-perovskite in super-earth mantles, Earth Planet. Sci. Lett. **478**, 40 (2017).

[11] L. Cobden, J. Zhuang, W. Lei, R. Wentzcovitch, J. Trampert, and J. Tromp, Full-waveform tomography reveals iron spin crossover in earth's lower mantle, Nat. Commun. **15**, 1961 (2024).

[12] R. M. Wentzcovitch, J. F. Justo, Z. Wu, C. R. S. Da Silva, D. A. Yuen, and D. Kohlstedt, Anomalous compressibility of ferropericlase throughout the iron spin cross-over, Proc. Natl. Acad. Sci. USA **106**, 8447 (2009).

[13] Z. Wu, J. F. Justo, and R. M. Wentzcovitch, Elastic anomalies in a spin-crossover system: Ferropericlase at lower mantle conditions, Phys. Rev. Lett. **110**, 228501 (2013).

[14] J. Zhuang and R. Wentzcovitch, Fe^{2+} Partitioning in Al-free pyrolite: Consequences for seismic velocities and heterogeneities, Geophys. Res. Lett. **51**, e2024GL108967 (2024).

[15] T. Katsura, K. Sato, and E. Ito, Electrical conductivity of silicate perovskite at lower-mantle conditions, Nature (London) **395**, 493 (1998).

[16] Y. Xu, C. McCammon, and B. T. Poe, The Effect of alumina on the electrical conductivity of silicate perovskite, Science **282**, 922 (1998).

[17] J. Badro, J. P. Rueff, G. Vankó, G. Monaco, G. Fiquet, and F. Guyot, Electronic transitions in perovskite: Possible nonconvecting layers in the lower mantle, Science **305**, 383 (2004).

[18] I. I. Mazin and V. I. Anisimov, Insulating gap in FeO: Correlations and covalency, Phys. Rev. B **55**, 12822 (1997).

[19] M. Cococcioni and S. de Gironcoli, Linear response approach to the calculation of the effective interaction parameters in the LDA+U method, Phys. Rev. B **71**, 035105 (2005).

[20] A. Georges, G. Kotliar, W. Krauth, and M. J. Rozenberg, Dynamical mean-field theory of strongly correlated fermion systems and the limit of infinite dimensions, Rev. Mod. Phys. **68**, 13 (1996).

[21] N. Lanatà, T. H. Lee, Y. X. Yao, V. Stevanović, and V. Dobrosavljević, Connection between Mott physics and crystal structure in a series of transition metal binary compounds, npj Comput. Mater. **5**, 30 (2019).

[22] A. O. Shorikov, Z. V. Pchelkina, V. I. Anisimov, S. L. Skornyakov, and M. A. Korotin, Orbital-selective pressure-driven metal to insulator transition in FeO from dynamical mean-field theory, Phys. Rev. B **82**, 195101 (2010).

[23] V. I. Anisimov, J. Zaanen, and O. K. Andersen, Band theory and Mott insulators: Hubbard U instead of stoner I, Phys. Rev. B **44**, 943 (1991).

[24] A. I. Liechtenstein, V. I. Anisimov, and J. Zaanen, Density-functional theory and strong interactions: Orbital ordering in Mott-Hubbard insulators, Phys. Rev. B **52**, R5467(R) (1995).

[25] H. J. Kulik, M. Cococcioni, D. A. Scherlis, and N. Marzari, Density functional theory in transition-metal chemistry: A self-consistent Hubbard U approach, Phys. Rev. Lett. **97**, 103001 (2006).

[26] M. Cococcioni and N. Marzari, Energetics and cathode voltages of $LiMPO_4$ olivines (M = Fe, Mn) from extended Hubbard functionals, Phys. Rev. Mater. **3**, 033801 (2019).

[27] A. Floris, I. Timrov, B. Himmetoglu, N. Marzari, S. de Gironcoli, and M. Cococcioni, Hubbard-corrected density functional perturbation theory with ultrasoft pseudopotentials, Phys. Rev. B **101**, 064305 (2020).

[28] H. Hsu, K. Umemoto, Z. Wu, and R. M. Wentzcovitch, Spin-state crossover of iron in lower-mantle minerals: Results of DFT+U investigations, Rev. Mineral. Geochem. **71**, 169 (2010).

[29] Y. Sun, M. Cococcioni, and R. M. Wentzcovitch, LDA+Usc calculations of phase relations in FeO, Phys. Rev. Mater. **4**, 063605 (2020).

[30] T. Tsuchiya, R. M. Wentzcovitch, C. R. S. da Silva, and S. de Gironcoli, Spin transition in magnesiowüstite in earth's lower mantle, Phys. Rev. Lett. **96**, 198501 (2006).

[31] D. C. Wallace and H. Callen, Thermodynamics of crystals, Am. J. Phys. **40**, 1718 (1972).

[32] P. Giannozzi, O. Andreussi, T. Brumme, O. Bunau, M. Buongiorno Nardelli, M. Calandra, R. Car, C. Cavazzoni, D. Ceresoli, M. Cococcioni, N. Colonna, I. Carnimeo, A. Dal Corso, S. De Gironcoli, P. Delugas, R. A. Distasio, A. Ferretti, A. Floris, G. Fratesi, G. Fugallo *et al.*, Advanced capabilities for materials modelling with QUANTUM ESPRESSO, J. Phys.: Condens. Matter **29**, 465901 (2017).

[33] P. Giannozzi, S. Baroni, N. Bonini, M. Calandra, R. Car, C. Cavazzoni, D. Ceresoli, G. L. Chiarotti, M. Cococcioni, I. Dabo, A. Dal Corso, S. De Gironcoli, S. Fabris, G. Fratesi, R. Gebauer, U. Gerstmann, C. Gougoussis, A. Kokalj, M. Lazzeri, L. Martin-Samos *et al.*, QUANTUM ESPRESSO: A Modular and open-source software project for quantum simulations of materials, J. Phys.: Condens. Matter **21**, 395502 (2009).

[34] D. Vanderbilt, Soft self-consistent pseudopotentials in a generalized eigenvalue formalism, Phys. Rev. B **41**, 7892 (1990).

[35] K. Umemoto, R. M. Wentzcovitch, Y. G. Yu, and R. Requist, Spin transition in (Mg, Fe)SiO$_3$ perovskite under pressure, Earth Planet. Sci. Lett. **276**, 198 (2008).

[36] H. J. Monkhorst and J. D. Pack, Special points for Brillouin-Zone integrations, Phys. Rev. B **13**, 5188 (1976).

[37] I. Timrov, N. Marzari, and M. Cococcioni, Hubbard parameters from density-functional perturbation theory, Phys. Rev. B **98**, 085127 (2018).

[38] H. Hsu, P. Blaha, M. Cococcioni, and R. M. Wentzcovitch, Spin-state crossover and hyperfine interactions of ferric iron in MgSiO$_3$ perovskite, Phys. Rev. Lett. **106**, 118501 (2011).

[39] A. Togo and I. Tanaka, First principles phonon calculations in materials science, Scr. Mater. **108**, 1 (2015).

[40] T. Qin, Q. Zhang, R. M. Wentzcovitch, and K. Umemoto, QHA: A python package for quasiharmonic free energy calculation for multi-configuration systems, Comput. Phys. Commun. **237**, 199 (2019).

[41] J. Zhuang, H. Wang, Q. Zhang, and R. M. Wentzcovitch, Thermodynamic properties of ϵ -Fe with thermal electronic excitation effects on vibrational spectra, Phys. Rev. B **103**, 144102 (2021).

[42] T. Wan, Y. Sun, and R. M. Wentzcovitch, Intermediate spin state and the B1-B2 transition in ferropericlase, Phys. Rev. Res. **4**, 023078 (2022).

[43] N. D. Mermin, Thermal properties of the inhomogeneous electron gas, Phys. Rev. **137**, A1441 (1965).

[44] R. M. Wentzcovitch, J. L. Martins, and P. B. Allen, Energy versus free-energy conservation in first-principles molecular dynamics, Phys. Rev. B **45**, 11372 (1992).

[45] F. Marumo and Y. Syono, The crystal structure of Zn$_2$SiO$_4$-II, a high-pressure phase of willemite, Acta Cryst. **B27**, 1868 (1971).

[46] R. Dutta, S. J. Tracy, and R. E. Cohen, High-pressure order-disorder transition in Mg$_2$SiO$_4$: Implications for super-earth mineralogy, Phys. Rev. B **107**, 184112 (2023).

[47] R. Dutta, S. J. Tracy, R. E. Cohen, F. Miozzi, K. Luo, J. Yang, P. C. Burnley, D. Smith, Y. Meng, S. Chariton, V. B. Prakapenka, and T. S. Duffy, Ultrahigh-pressure disordered eight-coordinated phase of Mg$_2$GeO$_4$: Analogue for super-earth mantles, Proc. Natl. Acad. Sci. USA **119**, e2114424119 (2022).

[48] K. Umemoto and R. M. Wentzcovitch, *Ab initio* prediction of an order-disorder transition in Mg$_2$GeO$_4$: Implication for the nature of super-earth's mantles, Phys. Rev. Mater. **5**, 093604 (2021).

[49] H. Hsu and R. M. Wentzcovitch, First-principles study of intermediate-spin ferrous iron in the earth's lower mantle, Phys. Rev. B **90**, 195205 (2014).

[50] https://doi.org/10.37807/GBMF12801.

[51] T. Wan, Data for "Spin state of iron in $I\bar{4}2d-$type Mg$_2$SiO$_4$ at ultrahigh pressures" [Data set], Zenodo (2025), https://doi.org/10.5281/zenodo.15360414.